THE JOURNAL OF PHYSICAL CHEMISTRY C

Article

Cite This: J. Phys. Chem. C 2018, 122, 27507−27515

pubs.acs.org/JPCC

Dynamical Solvent Effects on the Charge and Reactivity of Ceria-Supported Pt Nanoclusters

Lucie Szabová,[†] Matteo Farnesi Camellone,[‡,∥] Fabio Negreiros Ribeiro,[‡,⊥] Vladimír Matolín,[§] Yoshitaka Tateyama,[†] and Stefano Fabris*[,‡]

[†]Center for Green Research on Energy and Environmental Materials (GREEN) and International Center for Materials Nanoarchitectonics (MANA), National Institute for Materials Science (NIMS), 1-1 Namiki, Tsukuba, Ibaraki 305-0044, Japan

[‡]CNR-IOM DEMOCRITOS, Istituto Officina dei Materiali, Consiglio Nazionale delle Ricerche, via Bonomea 265, I-34136 Trieste, Italy

[§]Faculty of Mathematics and Physics, Department of Surface and Plasma Science, Charles University, V Holešovičkách 2, 18000 Prague, Czech Republic

Supporting Information

ABSTRACT: Supported Pt nanoparticles are key components in heterogeneous catalysis for energy and environment applications that involve vapor and wet conditions. In the latter case, the reaction proceeds at the catalyst−water interface where the solvent actively participates in the reaction mechanism. In this work, ab initio molecular dynamics simulations shed light on the effects of solvation on the reactivity and electronic properties of Pt_6 nanocatalysts supported by ceria (CeO_2), a highly reducible oxide. The calculated trajectories show that H_2O molecules spontaneously dissociate at both the supported Pt_6 cluster and at the ceria surface already at T = 350 K. Water dissociation leads to hydroxylation of the ceria surface and, most importantly, to the selective decoration of the metal−oxide periphery with hydroxide ions, which are stabilized by solvent-induced electronic effects and which quickly diffuse to the interfacial Pt sites via Grotthus-like proton chains. The periphery of the metal−oxide interface is thus identified as the active region of ceria-supported Pt clusters in wet environments. Solvation is shown to drive dynamic charge transfers across the metal/oxide interface that modify the cluster charge, a key parameter of the catalyst reactivity.

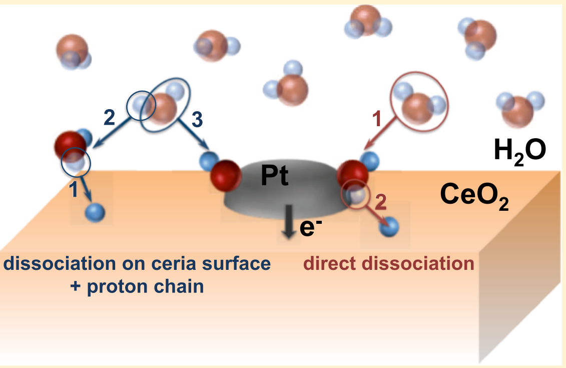

■ INTRODUCTION

The interaction between water and catalytic surfaces plays a crucial role in many technological applications, such as (photo-)electrochemical cells, environmental chemistry, or fuel cell technologies. A very significant field is the development of heterogeneous catalysis involving water-based approaches, which represent cheaper and safer alternatives to more traditional methods employing expensive and toxic solvents.[1] Complex reactions happen at solid−liquid interfaces where water, the most common solvent, takes active part in chemical reactions, affecting the charge and stability of surface adsorbates, reactants, and products, as well as of the relevant transition states.[2−7] The complexity of the atomistic and electronic processes occurring at these solid−liquid interfaces challenges fundamental experimental studies that require highly advanced in situ and in operando approaches. On the other side, material modeling can provide valuable fundamental insight, but it requires demanding dynamical approaches capable to sample the large configurational space of the solid−liquid interface.

Several ab initio molecular dynamics (AIMD) studies have recently focused on the interaction between water and catalytically relevant oxides surfaces, such as ZrO_2,[8] ZnO,[9,10] TiO_2,[11−13] GaP(001), InP(001),[14] and Fe_2O_3(001).[15] For the solid−liquid interfaces involving ZrO_2, ZnO, lnP(001), and Fe_2O_3, these studies show that interfacial water molecules dissociate already at room temperature, leading to surface hydroxy groups and to solvated hydroxide ions at the interface. The resulting hydroxide displays a dynamical equilibrium with interfacial water molecules that is governed by proton transfer between the hydroxide species, the partially hydroxylated surface sites, and the neighboring water molecules. This solvent-induced dynamics at the solid−liquid contact results in a very complex scenario where H_2O molecules, hydroxy groups and hydroxide ions play an important role in increasing the proton transfer rate and in accelerating the diffusion of reaction products or intermediates. For solid−liquid interfaces involv-

Received: September 19, 2018
Revised: October 31, 2018
Published: November 5, 2018

DOI: 10.1021/acs.jpcc.8b09154
J. Phys. Chem. C 2018, 122, 27507−27515

ing other oxides, such as TiO_2 surfaces, the interfacial water molecules do not dissociate because of the strong bonding with the five-fold coordinated Ti surface sites.[11]

The presence of supported catalytic clusters greatly increases the complexity of the catalyst and therefore represents an additional challenge to the simulations. For the paradigmatic case of TiO_2-supported Au clusters, it has been reported that gold particles larger than 4 nm, which are usually catalytically inert, show enhanced oxidation activity under aqueous conditions because of O_2 activation at the Au−liquid interface.[16] Indeed, the presence of moisture on Au/TiO_2 surfaces has been shown to increase the catalytic activity toward CO oxidation by orders of magnitude.[17] AIMD simulations showed that although water molecules do not dissociate at the solid−liquid interface, the solvent allows for stabilizing distinctive charge states of the metal nanoparticle that is shown to feature both "cationic" and "anionic" solvation depending on charge fluctuation and polarization effects.[12,13]

Here, we go beyond these studies by addressing metal nanoparticles supported by *highly reducible* oxide surfaces in wet chemical environments. We therefore consider a much more complex system including a supported metal nanoparticle at the water/oxide interface. In particular, we focus on the effects of the solvent on the charge, structure, and reactivity of Pt clusters supported by CeO_2 surfaces. Ceria is one of the most reducible oxides that is widely used in catalysis because of its high oxygen-storage capacity.[18−24] The improved reactivity of platinum−ceria catalysts can be traced back to the high reducibility of the ceria support and to the activation of the Pt catalyst through electron transfer at the metal−oxide contact. There is an extended literature addressing the structural and electronic properties of Pt clusters in the gas phase, particularly in the context of fuel cell catalysts,[25−28] but very little is known about *water-solvated* Pt/CeO_2 systems.

Recently, by AIMD simulations, we have investigated the impact of solvation on a CeO_2(111) surface in contact with liquid water showing that surface wetting strongly affects the equilibrium of water dissociation at the ceria/water contact.[29] Water dissociation yields a local increase of hydroxide OH^- ions and hydroxyl groups H^+ that activates the surface diffusion of hydroxide OH^- species via a Grotthus-like process. In the mentioned work, we included an example of how the Grotthus-like proton transport can provide a way for the dissociation products to transfer to and adsorb at the Pt cluster driving a charge transfer.

In this follow-up work, we extend our study to detailed analysis of the water solution effect on the ceria-supported Pt cluster. We describe the solvation pattern and solvent-induced charge transfer between the nanoparticle and the support as well as the water dissociation mechanisms at the $H_2O/Pt_6/CeO_2$ interface.

■ METHODS

The density functional theory calculations were performed using the Perdew−Burke−Ernzerhof (PBE)[34] generalized gradient-corrected approximation (GGA) for the exchange−correlation functional and ultrasoft pseudopotentials[35] for the electron−ion interactions as implemented in the Quantum-ESPRESSO computer package.[36] The spin-polarized Kohn−Sham equations were solved with a plane-wave basis cutoff of 30 Ry. It is well known that local and semi-local approximations to the XC functional fail to capture the correct insulating electronic structure of ceria-based materials, because of self-interaction effects arising from the Ce 4f electrons. The addition of an on-site Hubbard U term to the Hamiltonian has been shown to be an effective strategy to capture the atomistic and electronic structures of ceria-based materials.[37−44] In line with our previous works[30,45−47] we employed the GGA(PBE) + U approach in the implementation of Cococcioni and de Gironcoli[48] with a fixed value of U = 4.5 eV for the Ce f states. The occupations of the Ce f-states were computed by using atomic-like wave function projectors.

The Pt/CeO_2/water system was modeled with a Pt_6 cluster supported on a stoichiometric CeO_2(111) surface. We employed (4 × 4) supercell slabs with three O−Ce−O tri-layers to model the CeO_2(111) substrate. The Brillouin zone was sampled with the Γ-point, and the slabs were separated by more than 15 Å in the direction perpendicular to the surface (see Figure S1a,b). The initial lowest energy morphology of the supported Pt_6 cluster was determined in a previous work[30] that employed global optimisation algorithms. To model the Pt/CeO_2/water interface, the space between the slabs was filled with 66 H_2O molecules to obtain the effective density of water at p = 1 atm (1 g/cm^3) as displayed in Figure S1c.

The AIMD simulations were performed using the Car−Parrinello propagation scheme.[49,50] The canonical ensemble was sampled employing a fictitious mass 400 au for the electronic degrees of freedom, and the nuclear mass of deuterium was used for all H atoms. This allowed employing a time step of 0.12 fs for the integration of the equation of motions. The temperature of the nuclei was thermostated using Nosé−Hoover[51] chains at 350 K to establish the canonical ensemble; the orbital degrees of freedom were also coupled to Nosé−Hoover chains to ensure Car−Parrinello adiabaticity.

We have performed two sets of AIMD simulations. The first set simulated the gas-phase Pt_6/CeO_2 system for ∼15 ps, so as to generate a reference, solvent-free situation. In the second set, the Pt_6/CeO_2 system was solvated filling the vacuum space with 66 H_2 molecules as described above.

To study the dynamics, the following step-by-step procedure was adopted. First, all the atoms of the CeO_2 slab were kept fixed and the water molecules were allowed to relax. The system was then equilibrated with a *NVT* simulation at 350 K. A further equilibration step was applied, by repeating the *NVT* simulation and by allowing the movement of all the atoms in the supercell, except those in the lowest laying O−Ce−O trilayer, which were constrained to their equilibrium bulk-like positions. Finally, we have produced about 30 ps of equilibrated trajectories, which were used to achieve the results reported. Snapshots from the AIMD simulations were collected every ∼0.12 ps for electronic structure analysis.

The analysis of the charge rearrangement induced by the solvent at the oxide−liquid interface was performed by computing the Bader charges for selected species along the simulated trajectory. We quantify the charge rearrangement by introducing the following charge difference

$$\Delta \mathbf{Q}^{\alpha}(t;\, t_0) = \sum_{i=1}^{n_\alpha} \left(\mathbf{q}_i^{\alpha}(t) - \mathbf{q}_i^{\alpha}(t_0)\right) \tag{1}$$

where α indicates the given atomic species (Pt, Ce, O, ...) or water molecule, $\mathbf{q}_i^{\alpha}(t)$ and $\mathbf{q}_i^{\alpha}(t_0)$ are the charge of the i-th atom of species α (or i-th water molecule) at time t and at a reference time t_0, respectively. Overall, $\Delta\mathbf{Q}^{\alpha}(t)$ is a time-dependent measure of the charge difference for the species α

DOI: 10.1021/acs.jpcc.8b09154
J. Phys. Chem. C 2018, 122, 27507−27515

with respect to a reference value calculated at $t = t_0$. In the gas phase simulation, the reference snapshot t_0 is the one obtained after the initial structural and electronic optimization of the Pt_6/CeO_2 system. In the solvated case, the reference snapshot is selected from the AIMD trajectory before dissociation of any H_2O molecule. The quantity $\Delta \mathbf{Q}^{\alpha}(t)$ is used to quantify the time evolution of the charge rearrangement experienced by the system at the oxide−liquid interface.

Water molecules were considered as dissociated on the basis of interatomic distances between hydrogen (H), water oxygen (O^w), and surface oxygen (O^s) atoms. This allowed us to define the number of H^+ and OH^- species adsorbed at the interface upon water dissociation. A surface OH^- hydroxyl group is defined when the O^s−H^+ distance is smaller than 1.15 Å and hydroxide OH^- species is defined when one of the O^w−H distances is smaller than 1.3 Å, whereas all the others are larger than 1.3 Å. Analogously, a OH group results to be adsorbed at the Pt_6 cluster when the Pt−O distance is smaller than 2.3 Å.

■ RESULTS AND DISCUSSION

Pt_6/CeO_2 Gas-Phase System. We start by describing the time evolution of the structure and charge of the $Pt_6/CeO_2(111)$ system exposed to vacuum, that is without solvating water molecules. The starting configuration of these AIMD simulations was the fully optimised $Pt_6/CeO_2(111)$ system (see the Supporting Information and Figure S1a,b). The $Pt_6/CeO_2(111)$ model comprises five Pt interfacial atoms (denoted as Pt_I) that are in contact with the ceria surface, and one Pt atom (Pt_T) that occupies a face-centered cubic (fcc) position on top of the interfacial Pt_I layer. The cluster is strongly bound to the ceria surface with a calculated binding energy of 6.7 eV. This strong metal−support interaction is reflected in the electron transfer from the Pt cluster to the support that leads to the formation of three Ce^{3+} centers on the substrate.[30] The projected density of states (PDOS) and spin density analysis reveals that these three reduced Ce^{3+} ions are located on the uppermost trilayer of the $CeO_2(111)$ surface, at the cluster periphery (see inset in Figure 1a and ref 30).

We do not claim that the small size of Pt used in our simulations precisely reproduces the response to the solvent of larger and supported nanoparticles. The extensive AIMD simulations reported in this work could not be performed on larger clusters because they already required state-of-the-art highly parallelized software and large-scale high-performance computing facilities. We remark however that the value of our simulations is to provide a first description of the solvent effects on charge and reactivity for a small but well-defined Pt_6 cluster, through a careful comparison between its properties in vacuum and solvated.

Our first analysis of the AIMD trajectory focuses on the structural stability and dynamics of the supported Pt cluster. To this end, the Pt atomic positions were projected on a plane parallel to the surface every 1.2 fs. This defines the projected SDFs of the Pt atoms that are displayed in Figure 1b. This analysis shows that the thermal fluctuations of the interfacial Pt_I atoms are very small (mean squared displacement, MSD ≈ 0.4−0.5 Å), whereas the apical Pt_T atom clearly displays a larger mobility (MSD ≈ 0.7 Å). It occasionally diffuses to the other neighboring fcc sites, as evident from the SDF.

The analysis of the charge dynamics along the AIMD trajectory is displayed in Figure 1c). The blue and black lines

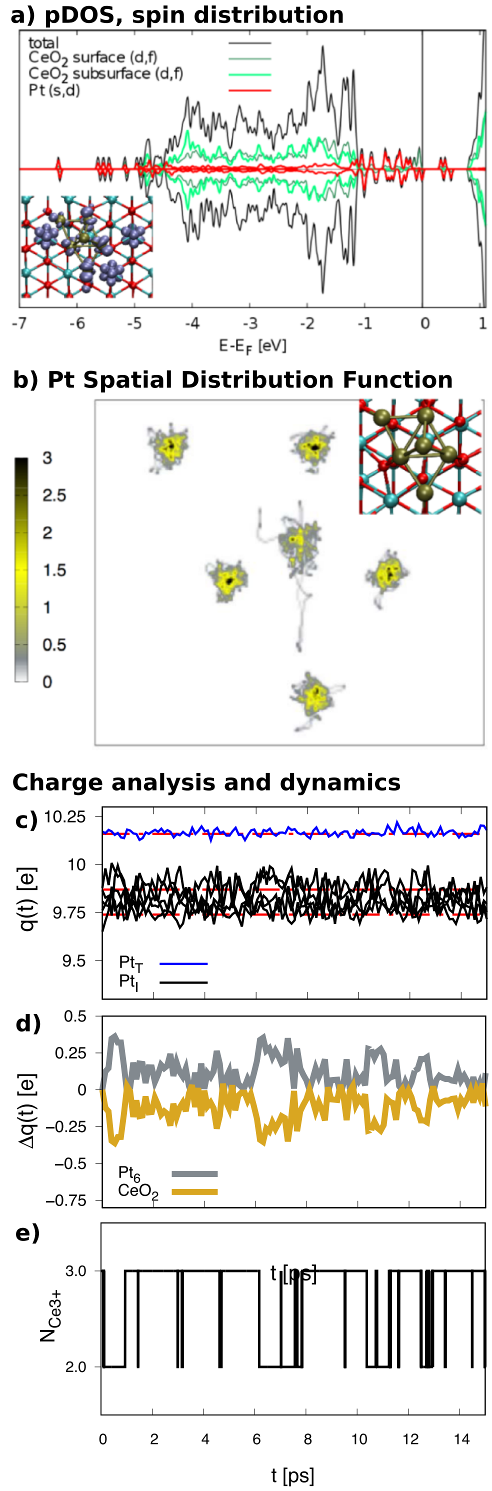

Figure 1. (a) Calculated DOS/PDOS of the $Pt_6/CeO_2(111)$ system in the gas phase and corresponding spin density plotted for the value 0.004 e/Å^3 (inset). (b) Spatial distribution functions (SDFs) of the Pt atoms of the supported Pt nanocluster projected onto the *xy* plane. The inset in panel (b) shows a representative snapshot extracted from the gas phase AIMD simulation. Time evolution of the Bader charges of Pt_T and Pt_I atoms (panel c), of the Pt_6 cluster and of the ceria substrate (d), and of the number of Ce^{3+} ions in the CeO_2 surface (e). Horizontal lines in panel (c) correspond to the values of Bader charges of the Pt_T atom and the range of values of the Pt_I atoms in the equilibrium lowest energy configuration.

DOI: 10.1021/acs.jpcc.8b09154
J. Phys. Chem. C 2018, 122, 27507−27515

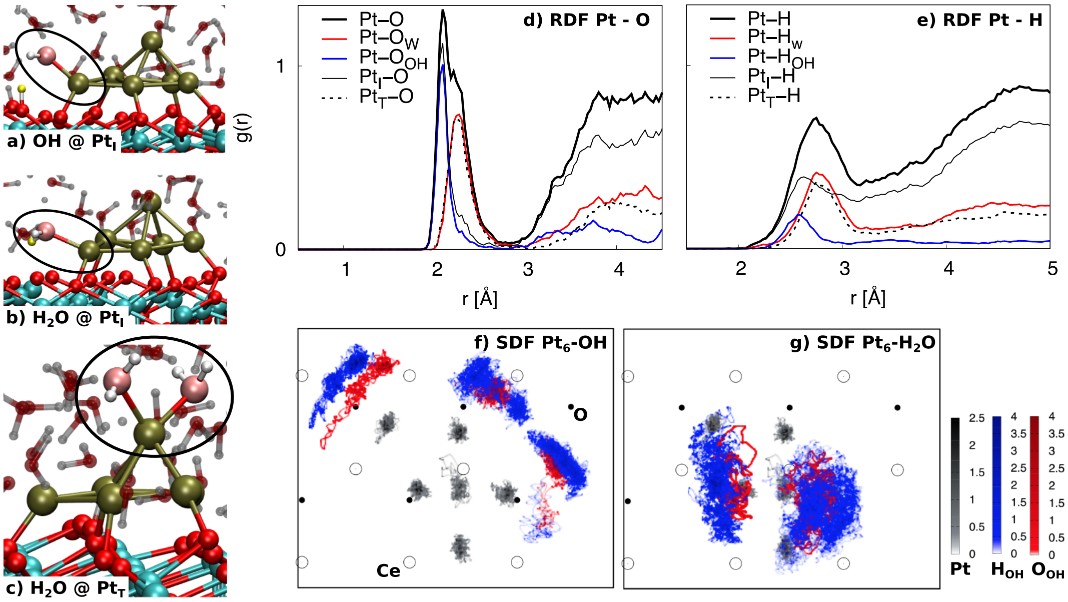

Figure 2. Representative AIMD configurations showing an interfacial Pt_I site coordinating (a) hydroxide and (b) water species, and (c) the apical Pt_T site coordinating two water molecules. (d) Pt−O and (e) Pt−H radial distribution functions (RDFs) and their deconvolution into individual components involving the Pt_T and Pt_I sites and the O atoms from water (O_W) and hydroxide (O_{OH}) species. SDFs projected on the *xy* plane of (f) Pt atoms and OH species, and (g) Pt atoms and H_2O species.

report the computed Bader charges of the Pt_T and Pt_I atoms, respectively. The horizontal-dashed lines represent the Bader charge values calculated at the equilibrium positions. Overall, the cluster is polarized with a clear charge depletion at the interfacial Pt_I atoms with respect to the apical Pt_T atom (time average of the Bader charges $\langle \mathbf{q}^{Pt_I} \rangle = 9.8$ |e|; $\langle \mathbf{q}^{Pt_T} \rangle = 10.2$ |e|). The Pt_T Bader charge is compatible with the one calculated in the bulk phase ($\langle \mathbf{q}^{Pt_{bulk}} \rangle = 10$ |e|), and its fluctuations are four times smaller than those of the Pt_I charges. The reason of this difference is in the interfacial charge dynamics/transfer that is activated by the thermal fluctuations of the Pt and CeO_2 atoms.

This is shown more clearly by plotting the collective Bader charge differences of the Pt_6 and CeO_2 systems, $\Delta \mathbf{Q}^{Pt_6}(t)$ and $\Delta \mathbf{Q}^{CeO_2}(t)$, respectively, that are reported in Figure 1d) as a function of time. These differences are defined with respect to the reference Bader charges computed at the beginning of the production trajectory (see Methods). The time-evolution of $\Delta \mathbf{Q}^{Pt_6}(t)$ (grey line) does not fluctuate regularly around an average value but it displays sharp transitions, which are perfectly correlated with equivalent and opposite transitions in the charge of the CeO_2 support $\Delta \mathbf{Q}^{CeO_2}(t)$ (yellow line). Furthermore, the latter charge transitions correlate with the change in the number of reduced Ce^{3+} ions, $N_{Ce^{3+}}$, which are plotted in Figure 1e, and which fluctuates between 3 and 2.

Besides providing the reference to assess the effects of solvation on cluster properties, this analysis shows that, at room temperature, the charge of the supported Pt cluster is not constant. It dynamically fluctuates because of charge transfers across the metal/oxide interface of ≈1 electron, which are activated by the atomic displacements and which affect the degree of reduction of the ceria support.

Pt_6/CeO_2/Water System. Having established the electronic structure and dynamical properties of the Pt/CeO_2 gas-phase system, we now analyse the effect of solvation on the ceria-supported Pt cluster. To this end, we have performed extensive (∼30 ps) PBE + *U* AIMD simulations of the Pt_6/CeO_2/water system, (see the Supporting Information and Figure S1c). Representative snapshots of these AIMD simulations are displayed in Figure 2a−c).

We first analyze the structure of the solvation shell around the Pt_6 cluster in terms of the Pt−O RDF, displayed by the black line in Figure 2d. The black thick line indicates the total Pt−O RDF calculated between all the Pt atoms and all the O atoms of the solvent water molecules. This first peak in this Pt−O RDF provides insight into the solvation shell structure of the supported Pt cluster. It has two clear components at 2.09 and 2.24 Å, and it is well separated from the larger Pt−O contributions of bulk water molecules.

Our simulations show that the two components of the first solvation peak can be attributed to specific OH and H_2O species that bind selectively to different cluster sites. To demonstrate this, we deconvolute the Pt−O RDF into its components (Figure 2d) involving the interfacial (Pt_I−O, thin solid black line) and top (Pt_T−O, dashed line) Pt atoms, as well as the O atoms from dissociated (Pt−O_{OH}, blue line) and molecular (Pt−O_W, red line) water molecules. This analysis clearly demonstrates that hydroxide species binds preferentially to the interface Pt_I atoms, which give rise to the Pt−O RDF peak at 2.09 Å. One instance of this configuration is shown in Figure 2a, in which one of the interacting OH groups has been highlighted. Water molecules instead preferentially interact with the top Pt atom (Pt_T−O_W), which is the most metallic and the furthest away from the metal/oxide interface, leading to the peak at 2.24 Å. A representative configuration is shown in Figure 2c.

Although the interfacial Pt_I atoms stabilise mostly OH species, water molecules are stable on Pt_I sites for shorter times during our AIMD simulation run. This is evident in the Pt−O_W RDF, which displays a nonnegligible contribution to the 2.24 Å Pt−O peak. This contribution is because of those water molecules at the Pt_I cluster sites that undergo dissociation during the AIMD simulation. This demonstrates the active role of the periphery of the Pt/CeO_2 interface toward water

DOI: 10.1021/acs.jpcc.8b09154
J. Phys. Chem. C 2018, 122, 27507−27515

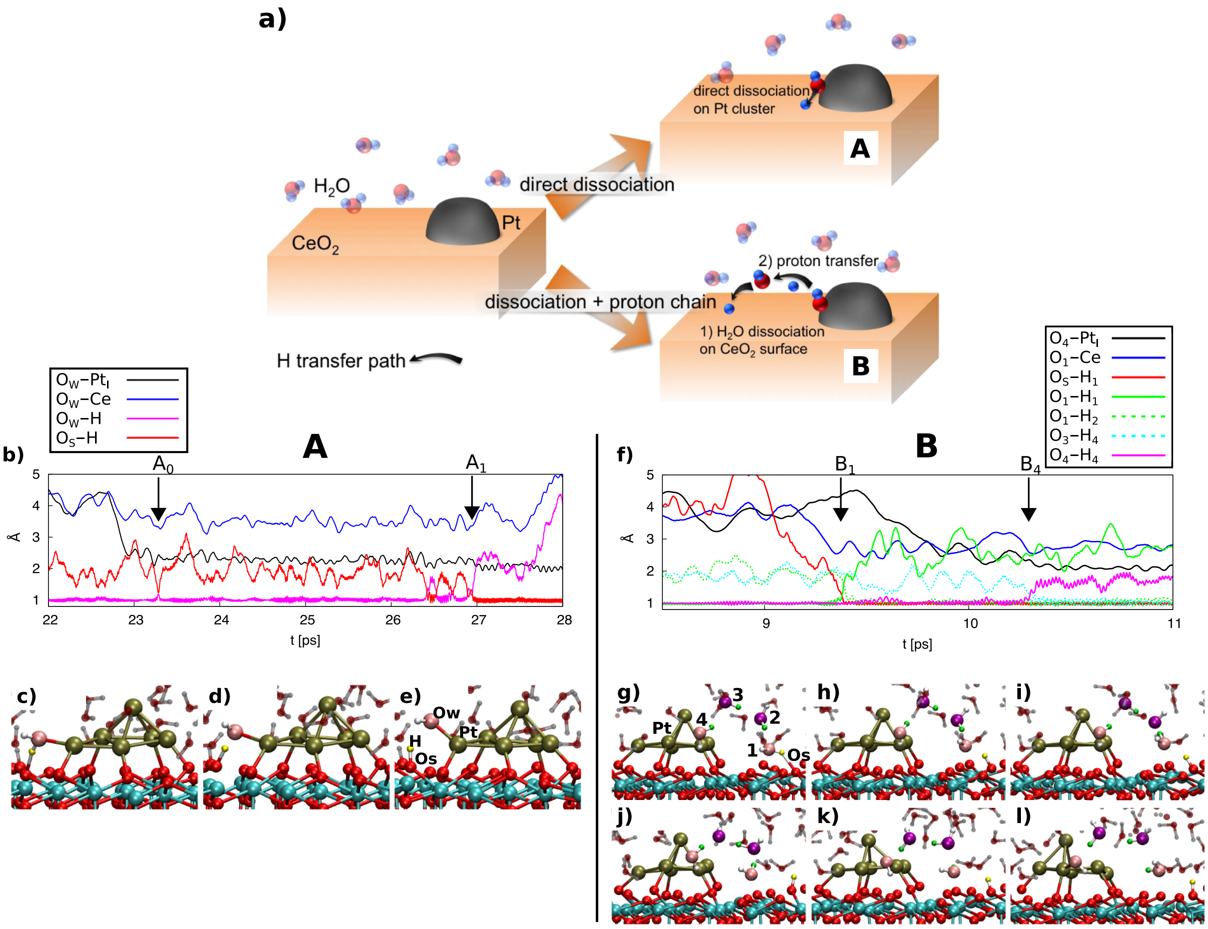

Figure 3. (a) Water dissociation pathways occurring at the Pt/ceria interface (A) and at the ceria surface (B). (b,f) Time evolution relevant bond lengths during water dissociation pathway A and B, respectively. Representative snapshots of the dissociation reactions A (c–e) and B (g–l).

dissociation, which will be discussed in the following. One instance of a metastable water molecule at the Pt/CeO_2 interface before dissociation is shown in Figure 2b. The proton that is transferred to the oxide support is displayed in yellow in Figure 2a,b. The conclusion that the interfacial Pt_I and metallic Pt_T atoms coordinate mostly OH and H_2O species, respectively, is further supported by the analysis of the Pt–H RDF (Figure 2e).

The structural analysis of the solvation shell resulting from the AIMD simulation points to a *cationic* solvation pattern of the Pt_6/CeO_2 system, that is the molecular and dissociated water molecules in the solvation shell point their O atoms toward the Pt_I and Pt_T sites. Note that this solely *cationic* solvation pattern differs from that one observed in AIMD simulations of other water-solvated oxide-supported metal clusters. For example, the solvation shell around the Au_{11}/TiO_2 system displays both *cationic* and *anionic* solvation pattern depending on the fluctuating charge state of the metal sites.[12,31] This dual solvation structure is not observed for the present $Pt_6/CeO_2/H_2O$ system and the reason can be traced back to the different polarisation of the solvated Au and Pt clusters. Two opposite charge states can be identified in the Au atoms of the solvated Au_{11}/TiO_2 system, which then stabilize the coexisting anionic and cationic solvation pattern. Only one charge state (positive) is instead predicted for the Pt atoms of the solvated $Pt_6/CeO_2/H_2O$ system, which therefore underpins the cationic solvation pattern. The cluster size may likely influence the latter cluster property.

The *xy*-projected SDFs calculated for Pt and hydroxide ions (Pt–O_{OH}), and for the Pt and H_2O molecules (Pt–O_W) are reported in Figure 2f,g, respectively. This analysis confirms the selective adsorption of hydroxide OH^- species to the interfacial Pt_I atoms and the preferential water coordination of the apical Pt_T atom. This selectivity is fully due to solvation because it is absent for the ceria-supported Pt cluster exposed to vacuum (see the Supporting Information).

This SDF analysis shows that solvation affects also the dynamics and structure of the supported Pt cluster. A direct comparison of the projected-SDFs of the solvated (Figure 2f,g) and gas-phase Figure 1b Pt cluster shows that the Pt_T apical atom occupies, on average, different positions with respect to the underlying Pt layer in contact with the oxide. When the supported Pt cluster is exposed to vacuum, the Pt_T atom is in an fcc site, thus binding to three neighboring Pt_I atoms. When the cluster is solvated, the interaction of the water molecules with the Pt_T atom displaces it to a lower-coordinated bridge site, thus binding to two neighboring Pt_I atoms.

Our simulations predict that water dissociation is activated by this Pt_6/CeO_2 solid/liquid interface already at T = 350 K. The analysis of the trajectories shows that two different dissociation mechanisms take place during the 30 ps of the AIMD run (A and B in Figure 3a). They differ in the active sites that promote the reaction: (A) direct water dissociation at the Pt_I site of the metal–oxide periphery, and (B) chain of water dissociations activated by the ceria surface. Note that both processes lead to the same final product, i.e., an OH

DOI: 10.1021/acs.jpcc.8b09154
J. Phys. Chem. C 2018, 122, 27507–27515

species bound to a Pt_I cluster site. These reaction mechanisms are analyzed by plotting the time evolution of selected bond lengths involved in the dissociation processes (Figure 3b,f).

Process A takes place between t = 23 and t = 27 ps. It begins with the binding of a water molecule to a Pt_I site, as seen from the shortening of the Pt_I−O_W distance (black line at time frame A_0) to ≈2.3 Å. The water molecule points its O_W atom to the Pt_I site, as displayed by the representative snapshot in Figure 3c. The water molecule dissociates after ≈3.5 ps (t = 27 ps, time frame A_1), via proton transfer to the closest surface O_S atom, as seen from the correlated O_S−H (red) shortening and O_W−H (purple) lengthening. Figure 3d,e displays the intermediate and final configurations that lead to the formation of the O_S−H and Pt_I−O_WH groups. We anticipate here that this dissociation process drives the charge transfer of ≈1 electron from the hydroxide species, to the Pt cluster and finally to the ceria surface (see below for details of the charge analysis).

Process B takes place between t = 9 and t = 11 ps. It involves a proton chain between four water molecules that mediate the diffusion of a hydroxide species from the ceria surface—which triggers the first dissociation—to the Pt_I site—which captures and immobilizes the hydroxide into a Pt_I−OH group. This complex interface reaction is described in Figure 3f in terms of the time evolution of interatomic distances involving protons H^+ and O atoms of the four participating water molecules, which are labeled H_i^+ and O_i with i = 1, ..., 4 (see Figure 3g). We omit here the W subscript.

The first water dissociation (t ≈ 9.4 ps, time frame B_1) takes place on the ceria surface at 10.2 Å away from the Pt cluster and involves the transfer of the H_1^+ proton to a surface O_S site. See the shortening (lengthening) of the O_S−H_1 (O_1−H_1) distance and the snapshot in Figure 3h). The resulting hydroxide $O_1H_1^-$ triggers the dissociation of a neighboring bulk water molecule, which transfers its proton to the $O_1H_1^-$ hydroxide and turns it back into a water molecule (see Figure 3i). This creates a new $O_2H_2^-$ hydroxide, which activates the same proton transfer described above with the neighboring water molecule 3 and leads to a new $O_3H_3^-$ hydroxide displayed in Figure 3j. Finally, the latter accepts a proton from the water molecule 4, which is close to the Pt_I site (see Figure 3k). This fourth water dissociation (B_4 in Figure 3f) and the related proton transfer takes place ≈1 ps after the first water dissociation B_1. It leads to the Pt_I−O_4H_4 species displayed in Figure 3l, which is the same product of dissociation mechanism A. The overall effect of this proton chain is to effectively transfer hydroxide ions from the ceria surface, where they are formed after water dissociation, to the periphery of the metal oxide. This fast hydroxide diffusion toward the supported Pt cluster is mediated by a Grotthus-like mechanism described before.[29] The charge transfer induced by the interaction of the hydroxide ion with the Pt_I site (see below) locks the Pt_I−OH product and prevents the reverse conversion to Pt_I−OH_2.

We now investigate the charge reorganization at the Pt/CeO_2/water interface induced by the solvent and by the water dissociation reactions. Similarly to the reference gas-phase system, the charge dynamics is analyzed in terms of time-dependent Bader charge differences $\Delta\mathbf{Q}^{Pt_6}(t)$, $\Delta\mathbf{Q}^{CeO_2}(t)$, $\Delta\mathbf{Q}^{H_2O}(t)$, and of the number of fully reduced Ce^{3+} ion (see Figure 4a,b, respectively). Panels (c−e) of the same figure report a statistical analysis of water dissociation in terms of the number of H and OH species interacting with the ceria substrate and Pt_6 cluster. The analysis of the charge dynamics

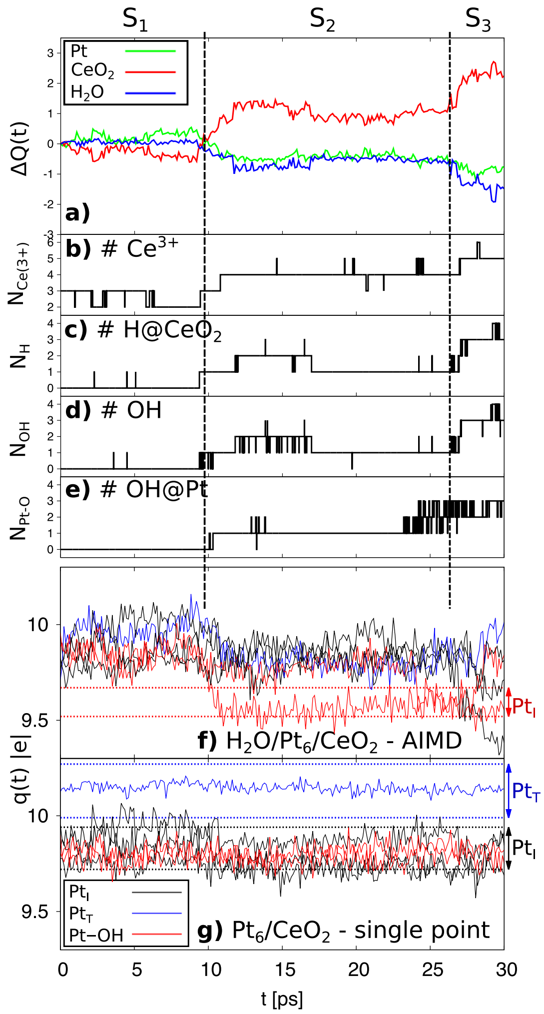

Figure 4. (a) Bader charge differences of the Pt_6 cluster, CeO_2 surface, and H_2O molecules. (b) Number of reduced Ce^{3+} ions on the ceria surface. Number of protons H^+ (c) and hydroxide OH^- groups (d). (e) Number of H_2O and OH species interacting with the Pt cluster. (f) Bader charges of Pt atoms in the solvated system and (g) in the corresponding gas phase system obtained by removing all the water molecules.

along the AIMD trajectory displayed in Figure 4 can be divided in three sections (labeled S_1, S_2, and S_3) according to the average values of Bader charge differences, with particular reference to $\Delta\mathbf{Q}^{H_2O}(t)$.

During the first 10 ps of the AIMD simulation (section S_1), the Bader charge differences $\Delta\mathbf{Q}^{Pt_6}(t)$ and $\Delta\mathbf{Q}^{CeO_2}(t)$ display fluctuations and sharp transitions that correlate with the number of Ce^{3+} ions in the ceria substrate (Figure 4a,b). These charge transitions in the cluster and substrate take place simultaneously and have opposite signs. The abrupt changes of average values in the $\Delta\mathbf{Q}^{Pt_6}(t)$ and $\Delta\mathbf{Q}^{CeO_2}(t)$ along the dynamics in section S_1 reflect the charge transfers of ≈1 e between the supported Pt cluster and the ceria substrate that are induced by the cluster/substrate dynamics. Quite importantly, water is not involved in these charge transfers: The solvent $\Delta\mathbf{Q}^{H_2O}(t)$ fluctuates around 0. Note that no water dissociation takes place during section S_1 of the trajectory.

Section S_2 (from t ≈ 10 ps to t ≈ 27 ps) of the AIMD simulation exhibits a different charge pattern. The charge analysis of Figure 4a clearly shows a significant charge transfer

DOI: 10.1021/acs.jpcc.8b09154
J. Phys. Chem. C 2018, 122, 27507−27515

from the solvent and supported Pt cluster to the ceria substrate. The analysis of the trajectory around t = 10 ps reveals that this event originates from the water dissociation B_1 described above which leads to the Pt_I−OH product (Figure 4). Hydroxide adsorption to the Pt_I cluster site drives the transfer of ≈1 electron to the substrate, thus increasing the average number of Ce^{3+} ions from 3 to 4 Figure 4b. This is further corroborated by the analysis reported in Figure 4c−e that highlights the correlation between the increase in the number of hydroxide species adsorbed to the Pt cluster and in the number of reduced Ce^{3+} species. With respect to the average values in section S_1, the Bader charge differences $\Delta\mathbf{Q}^{Pt_6}(t)$, $\Delta\mathbf{Q}^{CeO_2}(t)$, and $\Delta\mathbf{Q}^{H_2O}(t)$ change in Section B by −0.65, 1.27, and −0.59 e, respectively. Differently from the gas phase, the charge transfer does not involve only the Pt_6/CeO_2 system [red and green lines in Figure 4a but also the solvent water molecules (blue line). In particular, upon water dissociation and hydroxide adsorption, the charges of both the Pt_6 and hydroxide species decrease by ≈1 e, which is transferred to the ceria substrate and localizes on a Ce ion, reducing it to Ce^{3+}. Overall, the process can be described as:

$$\begin{aligned} &H_2O + O_S + Pt_6 + Ce^{4+} \\ &\quad \rightarrow O_S - H^+ + Pt_6 - OH^- + Ce^{4+} \\ &\quad \rightarrow O_S - H^+ + Pt_6 - OH + Ce^{3+} \end{aligned} \tag{2}$$

Note that the dissociation of H_2O molecules on the ceria surface in the absence of the Pt cluster does not reduce the ceria substrate as described in refs.[29,32,33] Therefore, the increase in the number of reduced Ce^{3+} ions is only related to the hydroxide interaction with the *solvated* Pt cluster and to the related charge transfer from the Pt_6−OH^- system to the ceria substrate.

At the beginning of the last part of the simulations (section S_3, from $t \approx 27.5$ ps to $t = 30$ ps), another water dissociation event takes place, which triggers the same set of charge-transfer processes described above for section S_2. The data reported in (Figure 4) show that, during section S_3, an additional hydroxide species binds to a Pt_I cluster site. It drives electron transfer from the cluster to the oxide substrate and leads to the appearance of another Ce^{3+} ion, that is further reducing the ceria substrate. As a result, the Bader charge differences $\Delta\mathbf{Q}^{Pt_6}(t)$, $\Delta\mathbf{Q}^{CeO_2}(t)$, and $\Delta\mathbf{Q}^{H_2O}(t)$ change with respect to the average values in section S_2 by −0.46, 1.30, and −0.84 e, respectively.

The effect of solvation on the cluster charge can be further assessed by comparing the Pt Bader charges computed in the presence and absence of the water molecules for the same Pt_6/CeO_2 configurations. This charge analysis can be done by performing two single-point self-consistent calculations for each selected snapshot of the AIMD trajectory: one calculation of the full Pt_6/CeO_2/water system, the other calculation of the Pt_6/CeO_2 excluding all the water molecules, that is in the same structural configuration of the Pt_6/CeO_2/water snapshot. The results for the Pt_6/CeO_2 solvated and in-vacuum are reported in Figure 4f,g, respectively.

Before water dissociation (section S_1), all the Pt Bader charges of the solvated cluster fluctuate over the same [9.6−10.2] e interval (Figure 4f). Instead, without solvating water, the Pt_T, and Pt_I Bader charges fluctuate around distinctively different ranges, [10.1,10.2] e and [9.6,10.1] e, respectively (Figure 4g). The latter result is in good agreement with the charge analysis performed on the AIMD dynamics of the Pt_6/CeO_2 system exposed to vacuum (see Figure 1c and red lines in Figure 4f). The solvated cluster is therefore much less polarised than in the gas phase because of the dielectric nature of the solvent and related screening.

After water dissociation (sections S_2 and S_3), in the solvated system, the Bader charge of the Pt_I atom binding an OH adsorbate decreases to [9.4−9.6 *e*], whereas the charge of all the other solvated Pt_I and Pt_T atoms remains in the [9.6, 10.2 *e*] range (Figure 4f). This specific charge depletion due to water dissociation is much weaker when removing the solvating water molecules [see Figure 4g and Supporting Information].

■ CONCLUSIONS

In conclusion, our extensive AIMD simulations allowed unveiling the solvent effects at the interface between water and a ceria-supported Pt cluster. We demonstrate that H_2O molecules can directly dissociate at the periphery of the supported nanoparticle into protons H^+ that hydroxylate the surface and hydroxide OH^- ions that selectively bind to the metal−oxide interfacial sites of the platinum cluster. We also observe that water molecules dissociate away from the nanoparticle, on the oxide surface, and that the resulting hydroxide species are quickly transferred to the same interfacial Pt sites via a Grotthus-like proton transfer chain mediated by interfacial solvent molecules. The two observed processes are accompanied by substantial charge reorganization at the metal oxide contact, resulting in charge transfer from the solvent and Pt cluster to the oxide support.

We can therefore conclude that solvation not only controls the selective binding of the OH^- species to the Pt_I sites at the periphery of the metal−oxide interface, but also determines the charge of the cluster, by driving electron transfer to the substrate that is proportional to the number of coordinating OH^- species. Moreover, the oxidation of the Pt−OH^- sites—coupled to the reduction of the Ce^{3+} underneath—locks the OH species to the cluster, preventing its back transformation into a solvent water molecule. Because the charge is a key parameter controlling reactivity of supported clusters, our results have general important implications in wet heterogeneous catalysis, with particular reference to hydrogenation/dehydrogenation and electro-chemical reactions.

■ ASSOCIATED CONTENT

Supporting Information

The Supporting Information is available free of charge on the ACS Publications website at DOI: 10.1021/acs.jpcc.8b09154.

Computational supercells and gas-phase properties of the Pt_6/CeO_2 system (PDF)

■ AUTHOR INFORMATION

Corresponding Author

*E-mail: fabris@iom.cnr.it.

ORCID

Lucie Szabová: 0000-0003-1901-1490
Matteo Farnesi Camellone: 0000-0001-9180-0115
Yoshitaka Tateyama: 0000-0002-5532-6134
Stefano Fabris: 0000-0003-2562-8788

Present Addresses

[∥]CERIC-ERIC S.S. 14—Km 163.5 in AREA Science Park, I-34139, Trieste (Basovizza), Italy.

[⊥]Universidade Federal do ABC, Av. dos Estados, 5001 Bairro Bangu, Santo André SP, CEP 09210-580 Brazil.

Notes

The authors declare no competing financial interest.

■ ACKNOWLEDGMENTS

This work was supported by the European Union via the FP7-NMP-2012 project chipCAT under contract no. 310191. S.F. acknowledges the support provided by the Humboldt Foundation through a Friedrich Wilhelm Bessel Research Award. L.S. and Y.T. thank the support by MEXT KAKENHI grant number JP15H05701. This research used computational resources of NIMS, Kyushu University and the HPCI systems through the HPCI System Research Projects (project IDs: hp170174, hp170169).

■ REFERENCES

(1) Sievers, C.; Noda, Y.; Qi, L.; Albuquerque, E. M.; Rioux, R. M.; Scott, S. L. Phenomena Affecting Catalytic Reactions at Solid-Liquid Interfaces. *ACS Catal.* **2016**, *6*, 8286−8307.

(2) Ping, Y.; Sundararaman, R.; Goddard, W. A., III Solvation Effects on the Band Edge Positions of Photocatalysts from First Principles. *Phys. Chem. Chem. Phys.* **2015**, *17*, 30499−30509.

(3) Pham, T. A.; Ping, Y.; Galli, G. Modelling Heterogeneous Interfaces for Solar Water Splitting. *Nat. Mater.* **2017**, *16*, 401−408.

(4) Björneholm, O.; Hansen, M. H.; Hodgson, A.; Liu, L.-M.; Limmer, D. T.; Michaelides, A.; Pedevilla, P.; Rossmeisl, J.; Shen, H.; Tocci, G.; et al. Water at Interfaces. *Chem. Rev.* **2016**, *116*, 7698−7726.

(5) Müller, P.; Wolf, P.; Hermans, I. Insights into the Complexity of Heterogeneous Liquid-Phase Catalysis: Case Study on the Cyclization of Citronellal. *ACS Catal.* **2016**, *6*, 2760−2769.

(6) Wang, H.; Sapi, A.; Thompson, C. M.; Liu, F.; Zherebetskyy, D.; Krier, J. M.; Carl, L. M.; Cai, X.; Wang, L.-W.; Somorjai, G. A. Dramatically Different Kinetics and Mechanism at Solid/Liquid and Solid/Gas Interfaces for Catalytic Isopropanol Oxidation over Size-Controlled Platinum Nanoparticles. *J. Am. Chem. Soc.* **2014**, *136*, 10515−10520.

(7) Rubasinghege, G.; Grassian, V. H. Role(s) of Adsorbed Water in the Surface Chemistry of Environmental Interfaces. *Chem. Commun.* **2013**, *49*, 3071−3094.

(8) Sato, R.; Ohkuma, S.; Shibuta, Y.; Shimojo, F.; Yamaguchi, S. Proton Migration on Hydrated Surface of Cubic ZrO_2: Ab Initio Molecular Dynamics Simulation. *J. Phys. Chem. C* **2015**, *119*, 28925−28933.

(9) Tocci, G.; Michaelides, A. Solvent-Induced Proton Hopping at a Water-Oxide Interface. *J. Phys. Chem. Lett.* **2014**, *5*, 474−480.

(10) Quaranta, V.; Hellström, M.; Behler, J. Proton-Transfer Mechanisms at the Water-ZnO Interface: The Role of Presolvation. *J. Phys. Chem. Lett.* **2017**, *8*, 1476−1483.

(11) Liu, L.-M.; Zhang, C.; Thornton, G.; Michaelides, A. Structure and Dynamics of Liquid Water on Rutile TiO_2(110). *Phys. Rev. B: Condens. Matter Mater. Phys.* **2010**, *82*, 161415.

(12) Farnesi Camellone, M.; Marx, D. On the Impact of Solvation on a Au/TiO_2 Nanocatalyst in Contact with Water. *J. Phys. Chem. Lett.* **2013**, *4*, 514−518.

(13) Muñoz-Santiburcio, D.; Farnesi Camellone, M.; Marx, D. Solvation-Induced Changes in the Mechanism of Alcohol Oxidation at Gold/Titania Nanocatalysts in the Aqueous Phase versus Gas Phase. *Angew. Chem.* **2018**, *57*, 3327−3331.

(14) Wood, B. C.; Schwegler, E.; Choi, W. I.; Ogitsu, T. Surface Chemistry of GaP(001) and InP(001) in Contact with Water. *J. Phys. Chem. C* **2014**, *118*, 1062−1070.

(15) English, N. J.; Rahman, M.; Wadnerkar, N.; MacElroy, J. M. D. Photo-Active and Dynamical Properties of Hematite (Fe_2O_3)-Water Interfaces: An Experimental and Theoretical Study. *Phys. Chem. Chem. Phys.* **2014**, *16*, 14445−14454.

(16) Shang, C.; Liu, Z.-P. Origin and Activity of Gold Nanoparticles as Aerobic Oxidation Catalysts in Aqueous Solution. *J. Am. Chem. Soc.* **2011**, *133*, 9938−9947.

(17) Daté, M.; Okumura, M.; Tsubota, S.; Haruta, M. Vital Role of Moisture in the Catalytic Activity of Supported Gold Nanoparticles. *Angew. Chem., Int. Ed.* **2004**, *43*, 2129−2132.

(18) Trovarelli, A. *Catalysis by Ceria and Related Materials*; Imperial College Press: London, 2002.

(19) Jacobs, G.; Williams, L.; Graham, U.; Thomas, G. A.; Sparks, D. E.; Davis, B. H. Low Temperature Water-Gas Shift: In Situ DRIFTS-Reaction Study of Ceria Surface Area on the Evolution of Formates on Pt/CeO_2 Fuel Processing Catalysts for Fuel Cell Applications. *Appl. Catal., A* **2003**, *252*, 107−118.

(20) Wang, X.; Rodriguez, J. A.; Hanson, J. C.; Gamarra, D.; Martínez-Arias, A.; Fernández-García, M. Ceria-Based Catalysts for the Production of H_2 through the Water-Gas-Shift Reaction: Time-Resolved XRD and XAFS Studies. *Top. Catal.* **2008**, *49*, 81−88.

(21) Kinch, R. T.; Cabrera, C. R.; Ishikawa, Y. A Density-Functional Theory Study of the Water−Gas Shift Mechanism on Pt/Ceria(111). *J. Phys. Chem. C* **2009**, *113*, 9239−9250.

(22) Kim, Y. T.; Park, E. D.; Lee, H. C.; Lee, D.; Lee, K. H. Water-Gas Shift Reaction over Supported Pt-CeO_x Catalysts. *Appl. Catal., B* **2009**, *90*, 45−54.

(23) Kašpar, J.; Fornasiero, P. Nanostructured Materials for Advanced Automotive De-pollution Catalysts. *J. Solid State Chem.* **2003**, *171*, 19−29.

(24) Bruix, A.; Lykhach, Y.; Matolínová, I.; Neitzel, A.; Skála, T.; Tsud, N.; Vorokhta, M.; Stetsovych, V.; Ševčíková, K.; Mysliveček, J.; et al. Maximum Noble-Metal Efficiency in Catalytic Materials: Atomically Dispersed Surface Platinum. *Angew. Chem., Int. Ed.* **2014**, *53*, 10525−10530.

(25) Bruix, A.; Rodriguez, J. A.; Ramírez, P. J.; Senanayake, S. D.; Evans, J.; Park, J. B.; Stacchiola, D.; Liu, P.; Hrbek, J.; Illas, F. A New Type of Strong Metal-Support Interaction and the Production of H_2 through the Transformation of Water on Pt/CeO_2(111) and Pt/CeO_x/TiO_2(110) Catalysts. *J. Am. Chem. Soc.* **2012**, *134*, 8968−8974.

(26) Lykhach, Y.; Kozlov, S. M.; Skála, T.; Tovt, A.; Stetsovych, V.; Tsud, N.; Dvořák, F.; Johánek, V.; Neitzel, A.; Mysliveček, J.; et al. Counting Electrons on Supported Nanoparticles. *Nat. Mater.* **2016**, *15*, 284−288.

(27) Lykhach, Y.; Bruix, A.; Fabris, S.; Potin, V.; Matolínová, I.; Matolín, V.; Libuda, J.; Neyman, K. M. Oxide-Based Nanomaterials for Fuel Cell Catalysis: The Interplay Between Supported Pt Atoms and Particles. *Catal. Sci. Technol.* **2017**, *7*, 4315−4345.

(28) Lykhach, Y.; Figueroba, A.; Farnesi Camellone, M.; Neitzel, A.; Skála, T.; Negreiros Ribeiro, F.; Vorokhta, M.; Tsud, N.; Prince, K. C.; Fabris, S.; et al. Reactivity of Atomically Dispersed Pt^{2+} Species towards H_2 Model Pt-CeO_2 Fuel Cell Catalyst. *Phys. Chem. Chem. Phys.* **2016**, *18*, 7672−7679.

(29) Farnesi Camellone, M.; Negreiros Ribeiro, F.; Szabová, L.; Tateyama, Y.; Fabris, S. Catalytic Proton Dynamics at the Water/Solid Interface of Ceria-Supported Pt Clusters. *J. Am. Chem. Soc.* **2016**, *138*, 11560−11567.

(30) Negreiros Ribeiro, F.; Fabris, S. Role of Cluster Morphology in the Dynamics and Reactivity of Subnanometer Pt Clusters Supported on Ceria Surfaces. *J. Phys. Chem. C* **2014**, *118*, 21014−21020.

(31) Farnesi Camellone, M.; Marx, D. Solvation of Au^+ *versus* Au^0 in Aqueous Solution: Electronic Structure Governs Solvation Shell Patterns. *Phys. Chem. Chem. Phys.* **2012**, *14*, 937−944.

(32) Fernández-Torre, D.; Kośmider, K.; Carrasco, J.; Ganduglia-Pirovano, M. V.; Pérez, R. Insight into the Adsorption of Water on the Clean CeO_2(111) Surface with van der Waals and Hybrid Density Functionals. *J. Phys. Chem. C* **2012**, *116*, 13584−13593.

(33) Marrocchelli, D.; Yildiz, B. First-Principles Assessment of H_2S and H_2O Reaction Mechanisms and the Subsequent Hydrogen

Absorption on the CeO_2(111) Surface. *J. Phys. Chem. C* **2012**, *116*, 2411−2424.
(34) Perdew, J. P.; Burke, K.; Ernzerhof, M. Generalized Gradient Approximation Made Simple. *Phys. Rev. Lett.* **1996**, *77*, 3865−3868.
(35) Vanderbilt, D. Soft Self-Consistent Pseudopotentials in a Generalized Eigenvalue Formalism. *Phys. Rev. B* **1990**, *41*, 7892−7895.
(36) Giannozzi, P.; Baroni, S.; Bonini, N.; Calandra, M.; Car, R.; Cavazzoni, C.; Ceresoli, D.; Chiarotti, G. L.; Cococcioni, M.; Dabo, I.; et al. Quantum ESPRESSO: A Modular and Open-Source Software Project for Quantum Simulations of Materials. *J. Phys.: Condens. Matter* **2009**, *21*, 395502.
(37) Paier, J.; Penschke, C.; Sauer, J. Oxygen Defects and Surface Chemistry of Ceria: Quantum Chemical Studies Compared to Experiment. *Chem. Rev.* **2013**, *113*, 3949−3985.
(38) Da Silva, J. L. F.; Ganduglia-Pirovano, M. V.; Sauer, J.; Bayer, V.; Kresse, G. Hybrid Functionals Applied to Rare-Earth Oxides: The Example of Ceria. *Phys. Rev. B: Condens. Matter Mater. Phys.* **2007**, *75*, 045121.
(39) Loschen, C.; Carrasco, J.; Neyman, K. M.; Illas, F. First-Principles LDA+U and GGA+U Study of Cerium Oxides: Dependence on the Effective U Parameter. *Phys. Rev. B: Condens. Matter Mater. Phys.* **2007**, *75*, 035115.
(40) Nolan, M.; Watson, G. W. The Surface Dependence of CO Adsorption on Ceria. *J. Phys. Chem. B* **2006**, *110*, 16600−16606.
(41) Zhang, C.; Michaelides, A.; King, D. A.; Jenkins, S. J. Structure of Gold Atoms on Stoichiometric and Defective Ceria Surfaces. *J. Chem. Phys.* **2008**, *129*, 194708.
(42) Ganduglia-Pirovano, M. V.; Da Silva, J. L. F.; Sauer, J. Density-Functional Calculations of the Structure of Near-Surface Oxygen Vacancies and Electron Localization on CeO_2(111). *Phys. Rev. Lett.* **2009**, *102*, 026101.
(43) Fabris, S.; Vicario, G.; Balducci, G.; de Gironcoli, S.; Baroni, S. Electronic and Atomistic Structures of Clean and Reduced Ceria Surfaces. *J. Phys. Chem. B* **2005**, *109*, 22860−22867.
(44) Fabris, S.; de Gironcoli, S.; Baroni, S.; Vicario, G.; Balducci, G. Taming Multiple Valency with Density Functionals: A Case Study of Defective Ceria. *Phys. Rev. B: Condens. Matter Mater. Phys.* **2005**, *71*, No. 041102(R).
(45) Ghosh, P.; Farnesi Camellone, M.; Fabris, S. Fluxionality of Au Clusters at Ceria Surfaces During CO Oxidation: Relationships among Reactivity, Size, Cohesion, and Surface Defects from DFT Simulations. *J. Phys. Chem. Lett.* **2013**, *4*, 2256−2263.
(46) Negreiros Ribeiro, F.; Farnesi Camellone, M.; Fabris, S. Effects of Thermal Fluctuations on the Hydroxylation and Reduction of Ceria Surfaces by Molecular H_2. *J. Phys. Chem. C* **2015**, *119*, 21567−21573.
(47) Szabová, L.; Tateyama, Y.; Matolín, V.; Fabris, S. Water Adsorption and Dissociation at Metal-Supported Ceria Thin Films: Thickness and Interface-Proximity Effects Studied with DFT+U Calculations. *J. Phys. Chem. C* **2015**, *119*, 2537−2544.
(48) Cococcioni, M.; de Gironcoli, S. Linear Response Approach to the Calculation of the Effective Interaction Parameters in the LDA+U Method. *Phys. Rev. B: Condens. Matter Mater. Phys.* **2005**, *71*, 035105.
(49) Car, R.; Parrinello, M. Unified Approach for Molecular Dynamics and Density-Functional Theory. *Phys. Rev. Lett.* **1985**, *55*, 2471−2474.
(50) Marx, D.; Hutter, J. *Ab Initio Molecular Dynamics: Basic Theory and Advanced Methods*; Cambridge University Press: New York, 2009.
(51) Nosé, S. Constant Temperature Molecular Dynamics Methods. *Prog. Theor. Phys. Suppl.* **1991**, *103*, 1−46.

DOI: 10.1021/acs.jpcc.8b09154
J. Phys. Chem. C 2018, 122, 27507−27515